Influence of the surface-to-bulk defects ratio of ZnO and TiO$_2$ on their UV-mediated photocatalytic activity

Christos A. Aggelopoulos [a],[*], Marinos Dimitropoulos [a],[b], Aikaterini Govatsi [a],[c],
Lamprini Sygellou [a], Christos D. Tsakiroglou [a], Spyros N. Yannopoulos [a],[*]

[a] Institute of Chemical Engineering Sciences, Foundation for Research and Technology Hellas (FORTH/ICE-HT), 26504 Patras, Greece
[b] University of Patras, Chemical Engineering Department, 26504 Patras, Greece
[c] University of Patras, Chemistry Department, 26504 Patras, Greece

ARTICLE INFO

ABSTRACT

Developing rational routes for nanoparticle synthesis with high photocatalytic (PC) efficiency is a mature field of research with yet unresolved issues. The presence of surface and bulk defects in the crystal structure is crucial as these exert different effect on the PC efficiency. However, understanding how the relative bulk-to-surface defects influence the PC activity is still missing. Mechanical activation (ball-milling) of ZnO nanoparticles is employed in this study as it provides a means to introduce lattice defects in a controlled way. The activated nano-powders were fully explored using techniques probing structure and optical properties. Notably, the defect density exhibits non-monotonic behavior against milling conditions. This unexpected behavior is interpreted by considering – the frequently overlooked fact – that various defect-probing techniques have different penetration depths into the particle volume; hence, each technique provides specific information on the relative bulk-to-surface defect ratio. Ball-milling appears to introduce mainly bulk defects as revealed by Raman scattering and X-ray diffraction. The kinetics of the PC activity on the degradation of methylene blue (MB) in water is in very good correlation with the defect density. Qualitative different results are obtained for TiO$_2$ nanoparticles where ball-milling engenders phase-transformation effects on the crystal lattice (phase transition and partial amorphization), while the PC activity in the MB degradation decreases also systematically with milling time. The current study provides some new insights into the issue of more reliable estimation of the bulk-to-surface defects ratio and their role on the PC activity of ZnO and TiO$_2$.

1. Introduction

The development of pure and modified photo-catalytically active nanomaterials, with potential use for water purification and disinfection, has been extensively studied for the degradation of most kinds of persistent organic pollutants, such as dyes, pesticides, chlorinated solvents and detergents, under UV, visible and solar irradiation [1–6]. Among the metal oxides used, TiO$_2$ has attracted most of the interest, whereas ZnO emerges over the last years as a very promising photocatalytic (PC) material for wastewater treatment, exhibiting even better photocatalytic activity than TiO$_2$ [7] attributed to its much higher electron mobility i.e. at least two orders of magnitude larger than that of TiO$_2$ [8]. However, both ZnO and TiO$_2$ exhibit moderate charge separation and quick recombination of photo-generated charge carriers, which leads to low reaction photoefficiency [9]. To alleviate this problem as well as to activate these semiconductors to solar irradiation, many efforts have been focused on the enhancement of the PC activity of TiO$_2$ and ZnO by increasing their visible light absorption; this has mostly been based on changing the electronic structure of the semiconductor [10–15]. On another front, certain studies have focused on the influence of structure defects on the PC efficiency of these oxides whose structure has been modified by changing particle shape and size, surface defects, etc. [16]. As defects play a key role in the fundamental phenomena involved in photocatalysis, particular emphasis has been placed on discriminating the effect of bulk and surface defects [17]. Surface defects have a twofold role serving as (i) charge carrier traps; hence, deteriorating PC activity and (ii) adsorption sites for the pollutant improving electron-hole separation. On the contrary, bulk defects serve only as charge carriers recombination sites [18]. Many studies revealed that surface oxygen vacancies created

by several methods (e.g. high temperature quenching, hydrogen thermal treatment, sonochemical process, etc.) [19–21] induced visible light absorption and enhanced the PC performance of TiO_2 [22,23] and ZnO [24,25]. However, contradictory results have been reported regarding the effect of bulk defects on the PC activity [26–28].

As defects play a dominant role of the lifetime and recombination rate of the photo-excited carriers, and taking into account that various kinds of defects exist in TiO_2 and ZnO such as oxygen vacancies, zinc/titanium interstitials, zinc vacancies and oxygen interstitials [29–31], it is challenging to understand how the type and concentration of defects affects the material PC performance. Furthermore, a thorough systematic comparison between the structural defects of TiO_2 and ZnO and their effect on the photocatalytic activity under UV irradiation is still lacking.

In this article we present a detailed investigation on the influence of defects, induced by high energy ball milling, on the PC activity of commercially available ZnO and TiO_2 (Degussa P25) nanoparticles. The PC activity was evaluated by the degradation of methylene blue (MB) from aqueous solutions in a lab-scale photocatalytic reactor under a UV light irradiation. The photocatalytic nanoparticles were characterized by a number of techniques such as SEM, XRD, Raman, UV–vis absorption, N_2 adsorption, PL and photoelectron spectroscopies (XPS/UPS). These techniques were employed in order to obtain information about the morphology (shape, size and aspect ratio), structure (crystal lattice, crystallinity and defects), other physicochemical properties (optical bandgap, photoluminescence, etc.) and surface chemistry of the photocatalytic materials. The combination of this information with the PC kinetics will shed light on the role of defects to the different PC activity between TiO_2 and ZnO.

2. Experimental section

2.1. Materials preparation

Commercial ZnO (Alfa Aesar, 99.8% purity) and TiO_2 (Degussa P25) powders were mechanically ground using a planetary milling instrument (Fritsch, model Pulverisette 7) operating at 400 rpm. Three different milling times were selected and the resulted activated nanopowders will be henceforth labeled as ZnO-0, ZnO-30, ZnO-60, and ZnO-180 for the 0, 30, 60, and 180 min milling time, respectively. Correspondingly, Degussa P25 TiO_2 powders were milled for the same times, hence following the labeling TiO_2-0, TiO_2-30, TiO_2-60, and TiO_2-300. The ball-to-mass ratio is 2:1, using 4 g of ZnO each time and 4:1 for TiO_2 using 1 g of TiO_2.

2.2. Morphological and optical characterization

The morphology of the ZnO and TiO_2 powders was characterized by field-emission scanning electron microscopy FE-SEM (Zeiss SUPRA 35VP-FEG) operating at 5 keV. Changes brought about in the crystal structure and particle size of the milled powders were examined by X- ray diffraction (XRD) using a Bruker D8 Advanced instrument operating with Ni-filtered CuKa1 radiation (λ = 0.154059 nm). The optical properties and hence the defect density of the nanostructures were investigated with the aid of photoluminescence spectroscopy (Hitachi F2500) employing a Xenon lamp operating at 325 nm as the excitation source. A narrow bandpass filter centered at 325 nm with full-width at half height of ~10 nm was used to improve the quality of the excitation light. Raman spectra were excited by a He-Cd laser operating at 441.6 nm. Backscattered light (through a microscope objective $50\times$) was analyzed by a single monochromator (Labram HR800, Jobin-Yvon) and detected by a liquid-nitrogen cooled CCD detector. The specific

surface area of the samples was measured with a N_2 adsorption analyzer (Micromeritics Gemini) by using the Brunauer-Emmett-Teller (BET) method.

2.3. Photoelectron spectroscopies

The surface analysis studies were performed in a UHV chamber (P < 10^{-9} mbar) equipped with a SPECS LHS-10 (EA10) hemispherical electron analyzer. The XPS measurements were carried out at room temperature using un-monochromatized AlKa radiation under conditions optimized for maximum signal (constant ΔE mode with pass energy of 36 eV giving a full width at half maximum (FWHM) of 0.9 eV for the Au 4f7/2 peak). The analyzed area was an ellipsoid with dimensions 2.5×4.5 mm^2. The XPS core level spectra were analyzed using a fitting routine, which allows the decomposition of each spectrum into individual mixed Gaussian-Lorentzian components after a Shirley background subtraction. The samples were in powder form and pressed into pellets. Wide Scans were recorded for all samples, while the core level peaks that were recorded were: Zn2p$_{3/2}$, C1s, O1s, and Zn Auger peak. The wide scans were recorded with pass energy of 97 eV. Errors in quantitative data are found in the range of ~10% (peak areas), while the accuracy for BEs assignments is ~0.1 eV. The binding energy reference for the electrostatic charging due to X-ray irradiation was the C1 s at 284.8 eV from the superficial carbon contamination. The surface charging in all samples was ~1 eV. The Ultra Violet Photoelectron Spectroscopy (UPS) studies were performed using HeI irradiation with hν = 21.22 eV produced by a UV source (model UVS 10/35). During UPS measurements the analyzer was working at the Constant Retarding Ratio (CRR) mode, with CRR = 10. A bias of −12.29 V was applied to the sample in order to avoid interference of the spectrometer threshold in the UPS spectra. The high and low binding energy and highest cutoff positions were assigned by fitting straight lines on the high and low energy cutoffs of the spectra and determining their intersections with the binding energy axis. Regarding measurement errors it should be noted that an error of ±0.05 eV is assigned to the absolute values for work function. In order to avoid charging effects due to the high intensity of the UV irradiation, the powders were dispersed in 3D water and drop-casted on indium tin oxide (ITO)-coated glass. The ITO substrates were previously subjected to oxygen plasma treatment (RF = 10.5 W, 20 min) to improve surface wetting and the coating homogeneity.

2.4. Photocatalytic activity experiments

The PC activity of the P25 TiO_2, pristine ZnO, ball-milled TiO_2 and ZnO samples was evaluated by the degradation of methylene blue in drinking water (MB, 1 mg L^{-1}) under UV light irradiation. All experiments were conducted in a PC reactor consisting of a cylindrical glass tube with double walls for water recirculation acting as thermostating jacket, whereas dry air was injected upwards at a constant flow rate (0.2 L min^{-1}) through the wastewater. The UV light source (8 W, 365 nm) was inserted inside a quartz cylinder, which was placed in the center of the glass tube. In each test, 40 mg of photocatalyst was dispersed in 200 mL of MB solution. The aqueous solution was sonicated for 1 h in the dark and then stirred for 1 h to establish adsorption-desorption equilibrium between MB and photocatalyst before being irradiated. During the experiment, several solution samples (2 mL) were collected at various PC treatment times, centrifuged for 15 min at 13,000 rpm (Thermo Scientific, Heraeus Megafuge 16) and then analyzed in a UV–vis spectrophotometer (Hitachi, U-3000) to determine the concentration of MB from its characteristic adsorption peak at 663 nm [32]. The MB photodegradation rate was defined as C/C_0, where C_0 and C are the MB concentrations before and after irradiation, respec-

tively. All PC experiments were conducted – at least – in duplicate with excellent reproducibility.

3. Results and discussion

3.1. Morphological and structural changes of mechanically activated ZnO and TiO₂ powders

Representative FE-SEM images of the morphology of the pristine and mechanically milled ZnO powders are presented in Fig. 1. For each case the inset image shows a magnified view of the ZnO particles. No clear conclusion can be drawn by inspecting these images as ball milling does not seem to drastically affect the average particle size, which is of about 200 nm. Indeed, only in the ZnO-180 we observe the existence of a larger fraction of small particles in comparison to the pristine, ZnO-0, powder.

More detailed structural information is provided by XRD, as Fig. 2 illustrates. Diffraction patterns over wide angle range for the ZnO powders are shown in Fig. 2(a) where all Bragg peaks coincide with the wurtzite-type ZnO reflections. A progressive peak intensity decrease and broadening are observed with increasing milling time; this is better visualized by the comparison of the ZnO-0 and ZnO-180 powders in Fig. 2(b). Fig. 2(c) shows the full-width at half maximum (FWHM) of the three more intense Bragg peaks (100, 002 and 101) obtained by fitting these peaks with Voight-type line profiles. For all three peaks, the data show a linear increase of the FWHM for the first 1 h of milling and some kind of saturation at longer grinding times. An estimation of particle size from XRD data can be provided using the Scherrer formula, $r = K \lambda / \beta \cos \theta$, where K is a constant (with a value near unity) reflecting the shape factor with value near unity, β is the FWHM of the Bragg peak, and θ is the angle in degrees. Estimating the mean particle sizes after averaging the results of the three dominant Brag peaks we obtain 111, 72, 43, and 34 nm for ZnO-0, ZnO-30, ZnO-60, and ZnO-180, respectively. Although these results show a drastic decrease of particle size, this is not supported by the FE-SEM images which show moderate size changes (see Table 1) upon increasing the grinding time. It is known that the Scherrer formula provides a lower bound of the particle size which, as many factors contribute to line broadening as is also the case here. Therefore, the peak broadening cannot be ascribed to particle size decrease or else increase of surface defects. Alternatively, even if the size has not appreciably decreased, bulk defect can still be created destroying lattice coherence length and thus contributing to the XRD peak broadening.

Contrary to the grinding-induced structural changes observed in ZnO powders, no measurable structural changes were recorded for the P25 TiO₂ nanoparticles as Fig. 3 reveals. The anatase-to-rutile is the main structural transformation that TiO₂ undergoes under mechanical activation, while partial amorphization has also been reported [33]. Under the milling condition of the current work we observe no change in the relative intensities of the anatase to rutile (cf. the intensities of the 25.2° and 27.4° bands) demonstrating that this transformation does not take place. On the other

hand, a notable decrease of the diffracted intensity takes place with increasing grinding time, which can be accounted for by invoking a crystalline-to-amorphous transformation. The defects induced in the course of this process have profound effects on the PC activity of mechanically activated TiO₂, as shown in Section 3.5.

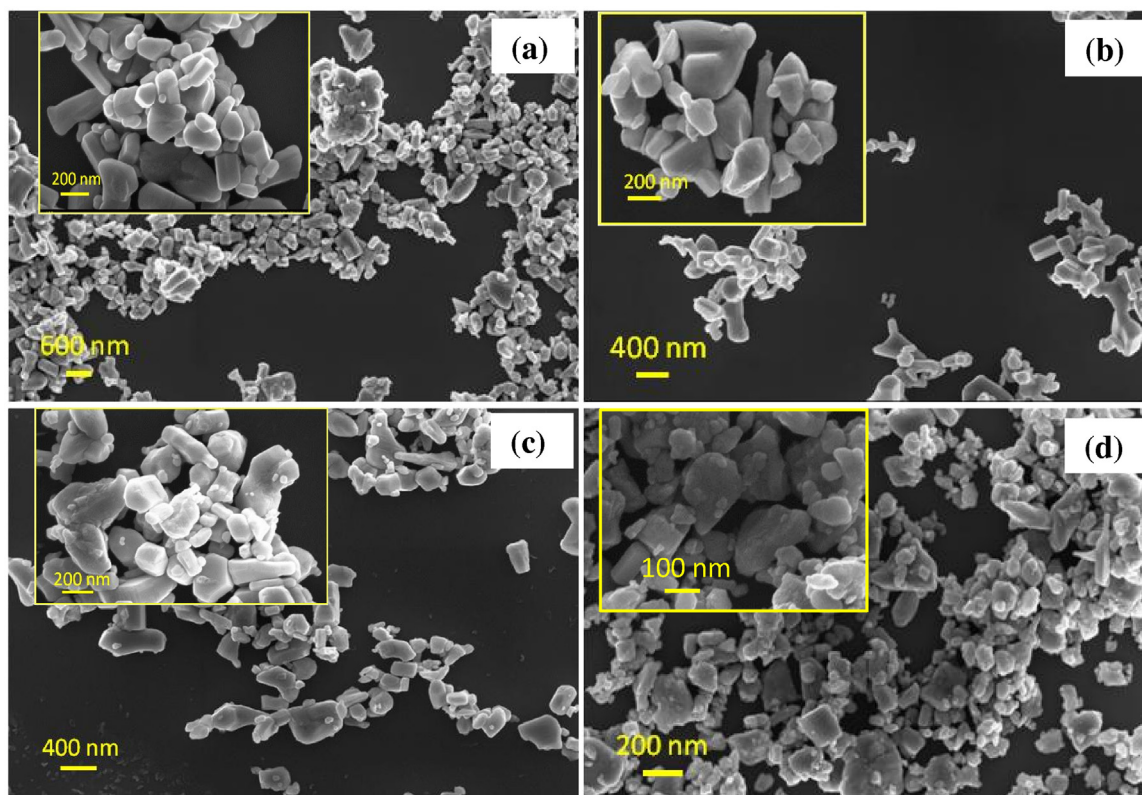### 3.2. Photoluminescence study of defects

Photoluminescence spectroscopy has proved a versatile technique for the study of defects of ZnO nanostructures [34]. Two main spectral ranges of interest are analyzed in the PL spectra. In the low energy region, 370–390 nm, a narrow band (UV band) dominates, assigned to the near-band edge emission of the wide band gap ZnO. A broader, composite band straddling the visible part (blue/green/red) of the spectrum corresponds to deep level emission originating from intra gap defects states. Fig. 4 shows representative PL spectra of the pristine and ball-milled ZnO powders. The spectra have been plotted in a way to present the UV-band at ~380 nm normalized to the same peak intensity among the various samples. This enables a more direct comparison between the relative intensities of the UV and visible band intensities. The PL spectrum of the bulk ZnO reveals the presence of very weak bands in the visible part of the spectrum, at ~440 and 530 nm, i.e. blue and green emission. The comparatively weak visible bands imply the presence of a low defect concentration.

Mechanical grinding of the pristine powder for 30 min, changes drastically the nature and concentration of defects and hence the form of the PL band. A broad band grows in the PL spectrum situated at ~540 nm. Analysis of this composite band into Gaussian-type lines reveals bands at 501, 541, and 570 nm. In addition, extra weak PL intensity, relative to the bulk, appears at ~410 nm. Blue/green emission is the most common emission from ZnO nanostructures. Several suggestions have been provided to account for the origin of the blue/green emission. Singly ionized oxygen vacancies, antisite oxygen, and zinc interstitials are the most common ones. Although the origin is still unclear, more solid experimental evidence shows that blue/green emission comes from the surface layers [35]. The spectral features at 540 and 410 nm appear with higher intensity in the ZnO-60 powder; this is reasonably expected after increasing the milling time as the concentration of the defects responsible for these bands increase. The individual lines composing the broad visible band are characterized by the same energies and the same relative intensities in comparison with the ZnO-30 PL spectrum. Unexpectedly, the intensity of the defect-related bands discussed above seems to decrease moderately for the powder milled for 3 h. However, both the XRD data (Fig. 2) and the analysis of the Raman spectra (following in Section 3.3) demonstrate that increasing the grinding time causes systematic changes in the crystal structure causing increasingly higher defect concentration.
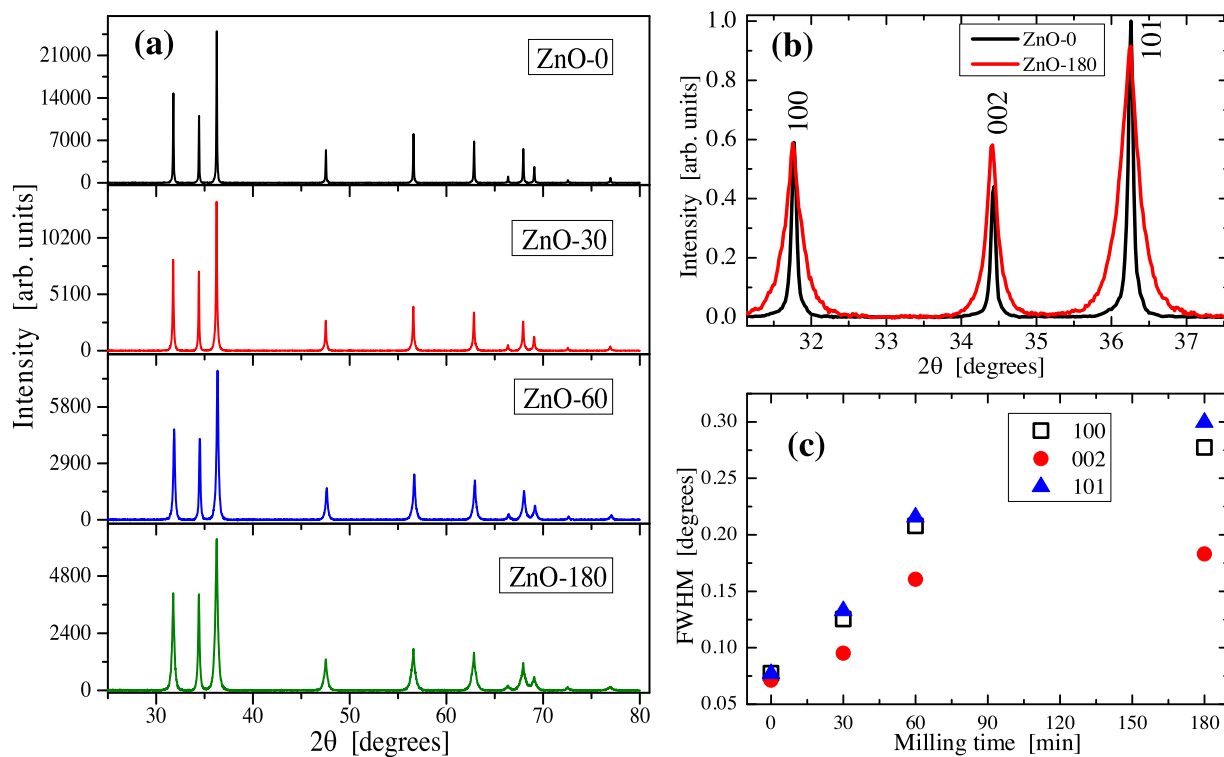
To account for the contrasting PL results of the ZnO-180 powder we should envisage the distinct role of the surface and bulk defects. On general grounds, the defect density on the surface is considered higher than in the bulk [36]. However, as the BET data show (see Table 1), ball milling does not substantially alter the surface area of the powders; only a slight increase is observed with prolonging grinding time. Therefore, mechanical activation is presumably causing bulk defects by distorting the crystal lattice. Increasing milling time, hence, modifies the ratio of bulk-to-surface defects. The question to be answered now pertains to why PL does not sense the bulk defects in the way that XRD and Raman scattering do. This can be accounted for by recalling that the penetration depth of the 325 nm radiation used to excite the PL spectra is of ca. 50 nm. Given that the ZnO particle size is of about 200 nm, this means that PL spectroscopy does not probe the whole range of bulk defects, unlike XRD and Raman spectroscopy which provide more accurate information for bulk defects in such large crystals.

Table 1
BET surface area and average size estimated from FE-SEM images of pristine and ball-milled TiO₂ and ZnO photocatalysts.

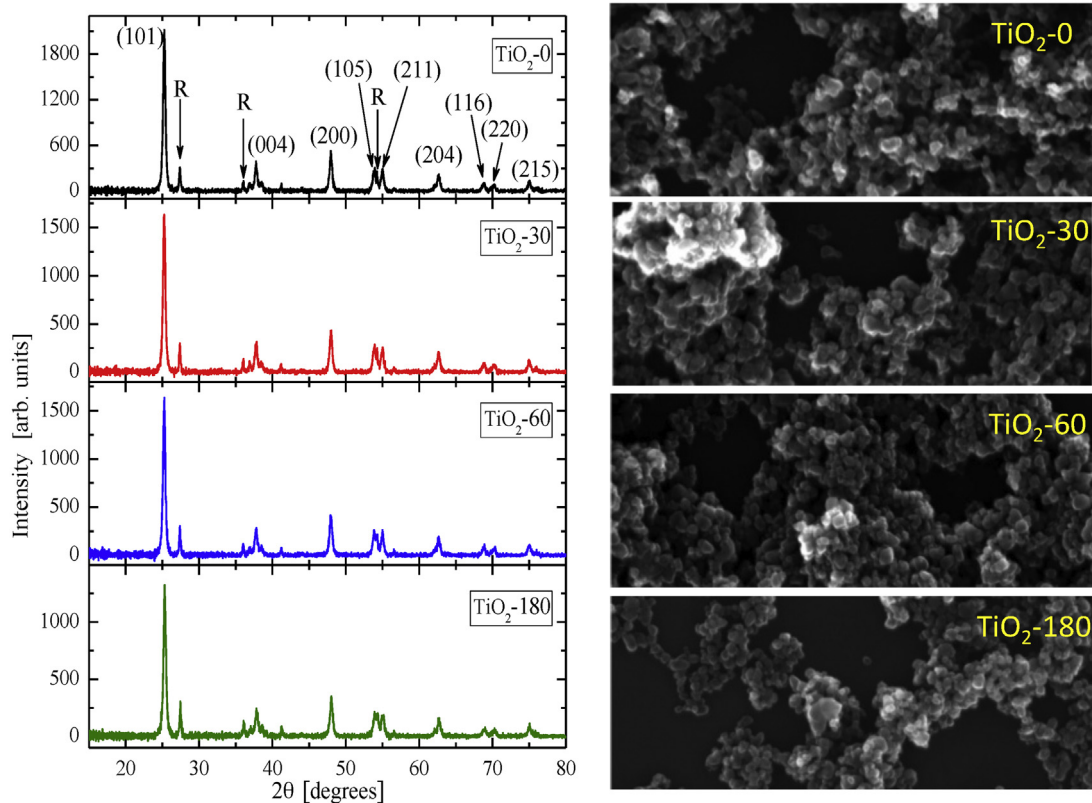| Samples	S_{BET} (m²/g)	Average Size (nm)
TiO₂-0	46.9	30 ± 5
TiO₂-30	46.3	30 ± 5
TiO₂-60	44.8	30 ± 5
TiO₂-180	44.1	30 ± 5
ZnO-0	4.1	200 ± 40
ZnO-30	4.2	200 ± 40
ZnO-60	4.3	180 ± 30
ZnO-180	5.6	150 ± 30

Fig. 1. Representative FE-SEM images of the pristine (a) and ground powders, ZnO-30 (b), ZnO-60 (c), and ZnO-180 (d). The insets show magnified views in each particular case.
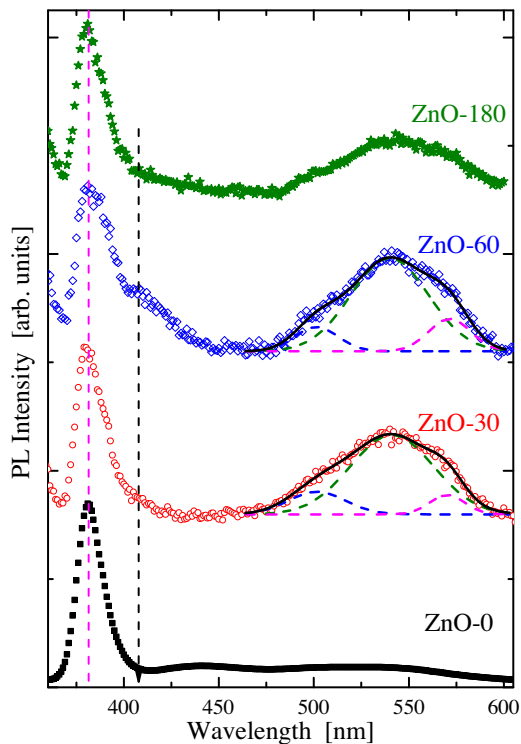

Fig. 2. (a) XRD patterns of the pristine and ball-milled ZnO powders; the ordinate shows the real diffraction intensity in each case. (b) Comparison of the shape of the three dominant Bragg peaks for the pristine and 3h-milled samples; the data have been normalized for clarity. (c) Dependence of the FWHM of the three dominant Bragg peaks on the milling time.
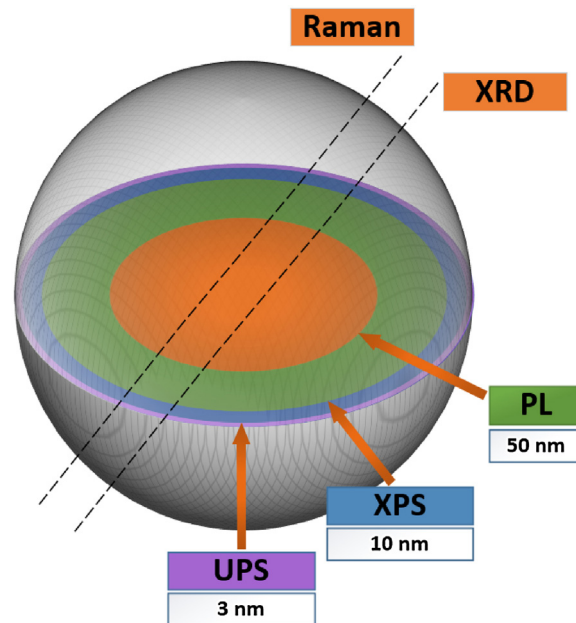
Fig. 3. XRD patterns (left) and FE-SEM images (right) of the pristine and ball-milled TiO$_2$ (P25) powders. The ordinate in the XRD patterns shows the real diffraction intensity in each case.

Fig. 4. PL spectra of the pristine and ball-milled ZnO powders.

Fig. 5. Schematic representation of the penetration depths of various defect-probing techniques in ZnO nanoparticles. Raman scattering far from resonance conditions and X-rays probe the whole particle volume. PL spectroscopy probes a shell of ~50 nm thick, while XPS/UPS are surface-sensitive probes.

Fig. 5 shows schematically the penetration depth of the radiation of various experimental techniques used to explore defects in ZnO nanoparticles.

3.3. Analysis of raman spectra

Fig. 6 shows representative Stokes-side Raman spectra of the pristine and ball-milled ZnO powders. The spectra have been normalized at the intensity of the E_2^{high} mode in order to help revealing
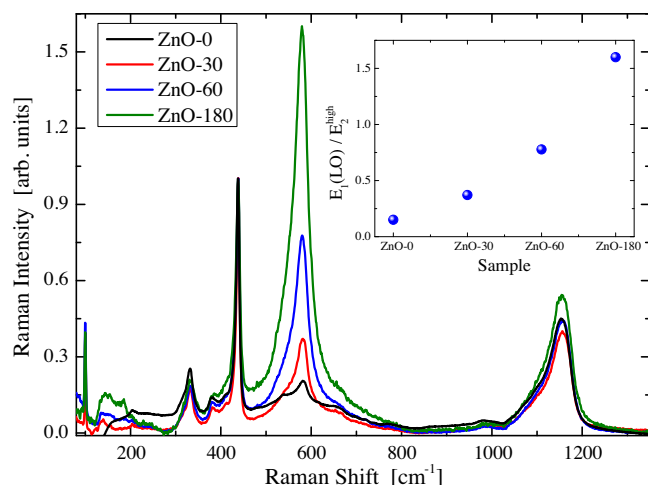
Fig. 6. Raman spectra of pristine and ball-milled ZnO nanoparticles.

Fig. 7. Raman spectra of pristine and ball-milled TiO$_2$ P25 nanoparticles. The arrows denote the appearance of the rutile-type peaks of TiO$_2$.

better the relative changes caused to other bands by mechanical milling. The intensity of the low energy band E_2^{low} located at ~100 cm^{-1} is suppressed by the notch filter effect which blocs the scattered intensity at frequencies lower than ~130 cm^{-1}. Crystalizing in the wurtzite-type structure ZnO is described by the C_{6v}^4 space group with two formula units in the primitive cell. The corresponding irreducible representation is given by the relation: $\Gamma = A_1 + 2B_1 + E_1 + 2E_2$, which implies six Raman-active modes in the first-order spectrum. The modes with B_1 symmetry are silent, while those with A_1 and E_1 symmetries are polar and split into transverse optical (TO) and longitudinal optical (LO) components. A detailed analysis of the Raman spectrum of ZnO has been reported by Arguello et al. [37] and Calleja et al. [38]. The frequencies and the symmetries of the Raman active modes are as follows. E_2^{low}: 101 cm^{-1}; A_1(TO): 380 cm^{-1}; E_1(TO): 413 cm^{-1}; E_2^{high}: 437 cm^{-1}; A_1(LO): 579 cm^{-1}; and E_1(LO): 590 cm^{-1}.

The main spectral changes observed in the Raman spectra of the milled powders is the systematic increase of the E_1(LO) mode as milling times increases. This mode exhibits an appreciable increase in relation to the E_2^{high} mode at long milling times. A detailed discussion on the relative intensity change of these two modes has been reported elsewhere [39] where the dependence of the intensity ratio E_1(LO)/E_2^{high} on the excitation wavelength revealed a dramatic increase of this ratio towards shorter wavelengths, as shown in the inset of Fig. 6. As discussed in [39] the E_1(LO) band is manifestation of the resonant enhancement of the LO mode due to the presence of extrinsic (doping) or intrinsic defects. In particular, resonance enhancement is observed here despite that the 2.8 eV laser line is sub-bandgap excitation. The origin of the effect lies on the activation of non-zero-centered optical phonons induced by defects in line with a model developed for extrinsic Fröhlich interaction (electron-phonon coupling). Therefore, the systematic increase of the E_1(LO)/E_2^{high} is in accord with an increasing defect concentration with increasing milling time.

The Raman spectra of pristine and ball-milled P25 TiO$_2$ are shown in Fig. 7 demonstrating the existence of rutile structure in all cases. The spectra have been normalized at the intensity maximum of the main band at ~144 cm^{-1}. This band shows weak broadening with increasing milling time; this particularly evident for the TiO$_2$-180 sample. The inset shows a magnification of the high energy bands in the spectral area 350–700 cm^{-1}. Practically, no observable spectral changes are observed between the pristine (TiO$_2$-0) and the powders ground for 30 and 60 min (TiO$_2$-30, TiO$_2$-60). The development of a broad background and moderate increase in the spectral areas designated by the arrows are observed in the case
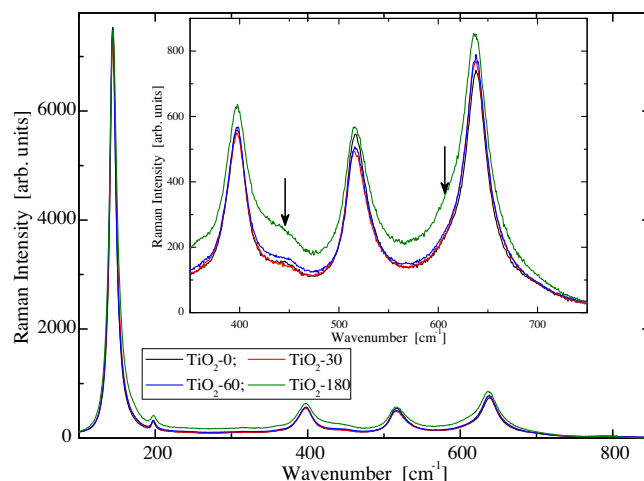
of the sample milled for 180 min. These weak bands at ~440 and ~605 cm^{-1} are manifestations of rutile type TiO$_2$. Previous studies [40] have revealed that mechanical grinding at appropriate conditions (ball-to-powder weight ratio ~40 and 700 rpm) is capable of complete transformation of anatase to rutile within 60 min of grinding. In the current study, the milling conditions (ball-to-powder weight ratio ~9 and 400 rpm) were not sufficient to induce the anatase-to-rutile transformation even for 180 min of milling. The broad background developed after 3 h of grinding is probably associated with the development of an amorphous phase as has also been inferred form the XRD data discussed previously.

3.4. XPS/UPS analysis

Survey scans for all samples revealed the presence of Zn, O and C peaks. Fig. 8a and b shows the Zn2p$_{3/2}$ XPS and Zn L$_3$M$_{45}$M$_{45}$ X-ray induced Auger Electron Spectroscopy (LMM XAES) spectra of the pristine and ground samples. The values of the binding energy at 1021.5 ± 0.1 eV, the Auger kinetic energy at 987.8 eV and consequently the modified Auger parameter α = 2010.2 ± 0.1 eV are in accord with stoichiometric ZnO [41].

The O1s photoelectron peak, shown in Fig. 9, is analyzed into three components: (i) a main peak at 530.2 eV assigned to oxygen in ZnO, (ii) a peak at 531.6 eV arising from surface adsorbed species such as carbonates/bicarbonates and hydroxyl species [42] and (iii) a weak peak at 532.6 eV associated to adsorbed water or other oxygen species. Surface hydroxyl species are adsorbed on defect sites and typically observed on ZnO surfaces even after Ar$^+$ sputtering or annealing [43]. The relative intensity ratio of the three analyzed components is practically the same for all samples within experimental error. An estimation of the stoichiometry took place by considering the intensity of Zn2p$_{3/2}$ and O1s peaks after weighting the peak areas by the appropriate relative sensitivity factor of each element having corrected it for the experimentally determined EA10 analyzer transmission characteristics. The atomic ratio O:Zn is about ~0.85 ± 0.05 (bulk and ZnO-30) and 0.75 ± 0.05 (ZnO-60 and ZnO180) indicating a slight increase of oxygen vacancies for the powders subjected to more severe mechanical treatment.

UPS was employed to provide information about the density and occupancy of electronic states in the valence band of the material. Fig. 10a shows the UPS of pristine and two of the ball-milled samples, i.e. ZnO-60 and ZnO-180. Table 2 compiles the values of the work function (WF) and the valence band edge (VBE) obtained by extrapolating the line of the secondary electron cut off and valence band region, respectively, as illustrated in Figs. 10b and c. The ion-
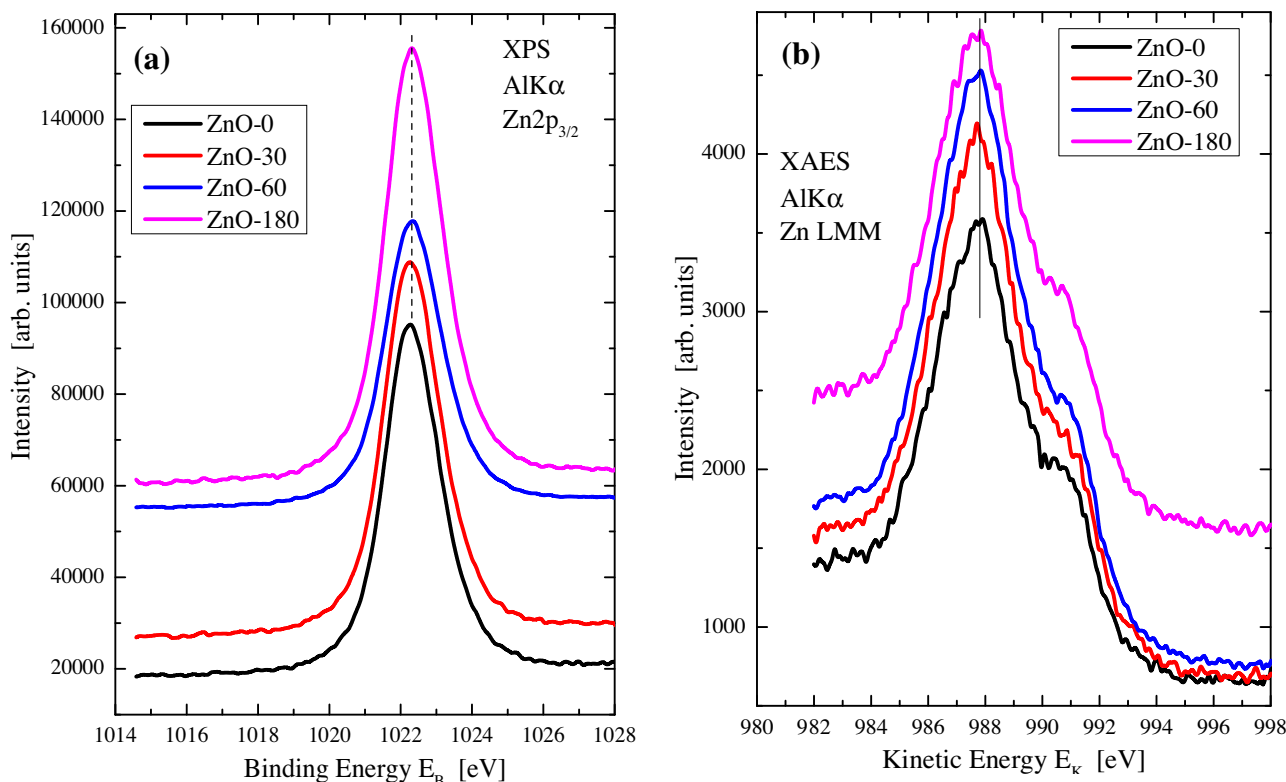
Fig. 8. XP Spectra of (a) Zn2p$_{3/2}$ and (b) X-ray induced Auger peak Zn LMM of ZnO-0, ZnO-30, ZnO-60 and ZnO-180 nanoparticles.
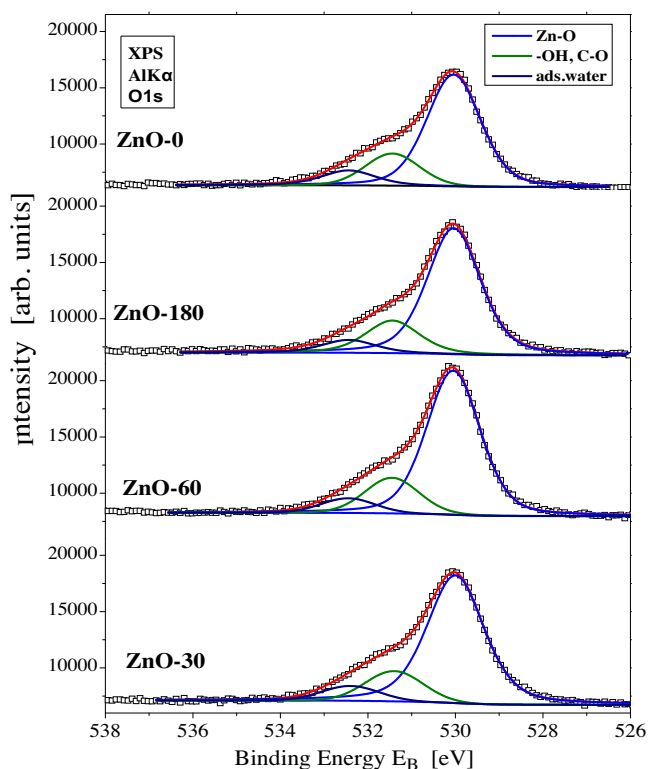

Fig. 9. Deconvoluted O1s X-ray photoelectron spectra of ZnO-0, ZnO-30, ZnO-60 and ZnO-180 nanoparticles.

ization potential values are also listed in Table 2. The magnitude of the work function and the valence band onset with respect to Fermi level (3.2 eV) manifest clearly the n-type nature of the powders.
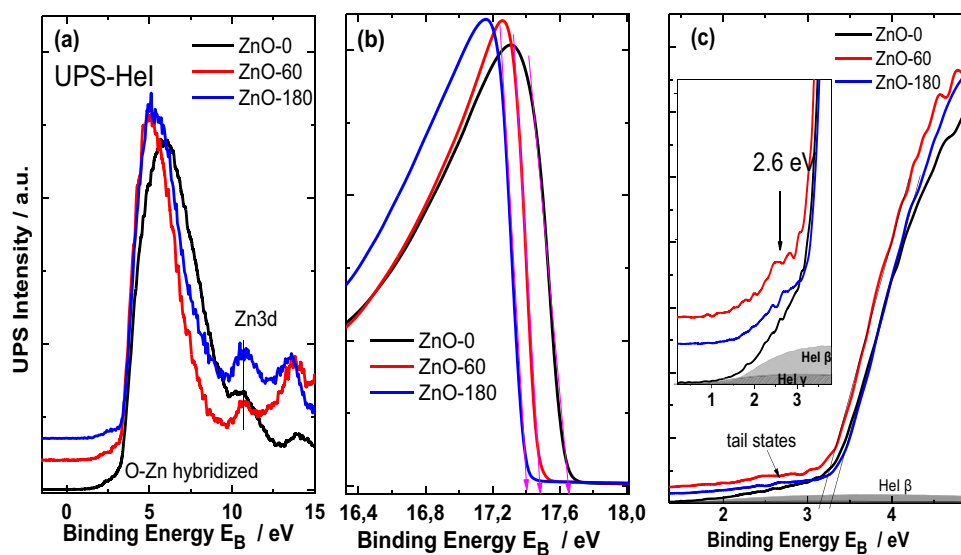
Table 2
Valence band edge, work function and ionization potential of the pristine and two ground ZnO samples.

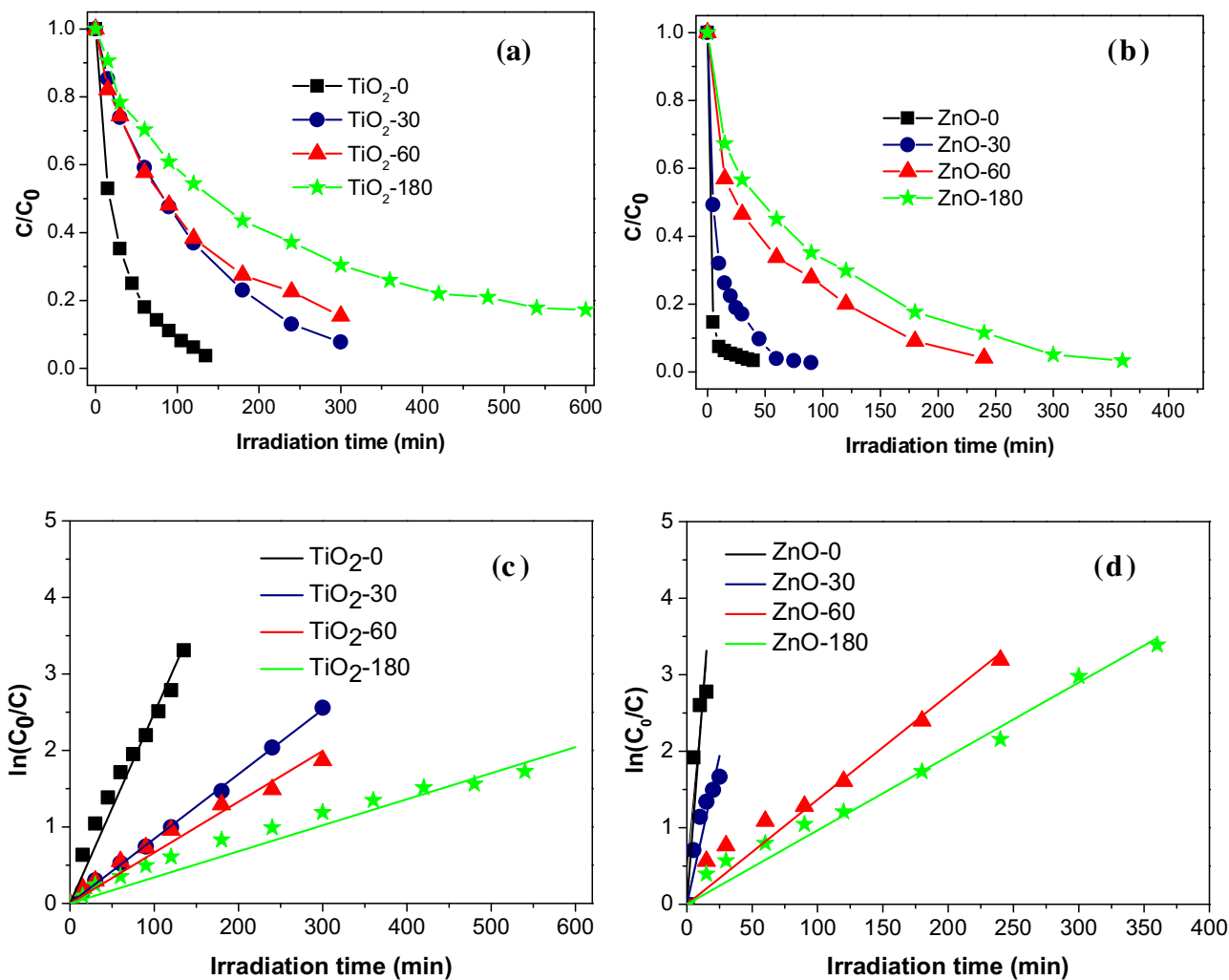| Sample	VBM/eV (±0.05)	WF/eV(±0.05)	IP/eV (±0.1)
ZnO-0	3.20	3.60	6.8
ZnO-60	3.10	3.70	6.8
ZnO-180	3.20	3.80	7.0

The valence band maximum is shown magnified in the inset of Fig. 10c. For the pristine sample (ZnO-0) the tail states near the Fermi level have been associated with deep lying defect levels such as Oxygen (O_v) and Zinc (Zn_V) vacancies [44]. The tail states lying on a continuous background created by a satellite emission from HeIβ and HeIγ are indicated in the Fig. 10(c) by the shaded areas. Their intensities are ∼2% and ∼0.5% of the HeIα signal, while their shift from the excitation is at 1.87 eV and 2.52 eV for the HeIβ and HeIγ signals, respectively [45]. For the mechanically milled samples a weak peak at ∼2.6 eV appears. This peak is attributed to the presence of defects in the bang gap of the zinc oxide [46] and has been associated with oxygen vacancies. We observe that the intensity of this peak decreases for the ZnO-180 powder in relation to the ZnO-60 sample, as is evidenced from the ZnO-180 spectrum in Fig. 10c. The lower intensity of the peak related to oxygen vacancies in the ZnO-180 than ZnO-60 is in accordance with the PL observation of a depleted defect-induced visible emission of the ZnO-180 sample.

3.5. Photocatalytic activity of TiO$_2$ and ZnO and influence of their defects

To evaluate the influence of defects on the PC activity of P25 TiO$_2$ and ZnO nanoparticles, a comparison of the photodegradation rate of the pristine and ball-milled powders at three different milling times (i.e. 30, 60 and 180 min) of the abovementioned pho-

Fig. 10. (a) UPS of pristine ZnO and ground powder for ZnO-60 and ZnO-180. (b) Secondary electron cut-off. (c) Valence band region and close-up of valence band maximum.

Fig. 11. Kinetics of the photodegradation of MB solution by pristine and ball milled (a) TiO$_2$ and (b) ZnO powders. The kinetic linear simulation curves of MB for the various (c) TiO$_2$ and (d) ZnO powders.
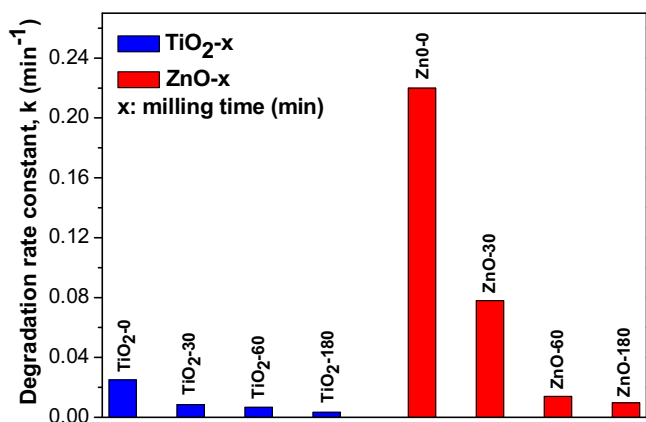
Fig. 12. Apparent rate constant k for the photodegradation of MB under UV irradiation over pristine and ball-milled TiO_2 and ZnO powders after 30, 60 and 180 min of milling.

tocatalysts was conducted. The PC activity was evaluated by the photodegradation of MB in drinking water under UV-365 nm irradiation. The evolution of the MB photocatalytic degradation rate as a function of time is shown in Fig. 11a and b for TiO_2 and ZnO powders, respectively.

Apparently, the pristine TiO_2 and ZnO powders exhibit better PC activity in the degradation of MB as compared with their ball-milled counterparts. Furthermore, the PC activity of the milled TiO_2 and ZnO samples shows systematic decrease as the ball-milling time increases. The degradation kinetics of MB was quantified by fitting the experimental data with the Langmuir-Hinshelwood model [47]:

$$ln\left(\frac{C_0}{C}\right) = kt \tag{1}$$

where k is the rate constant and C_0, C are the MB concentrations before and after UV irradiation, respectively. As shown in Fig. 11c and d, the photodegradation of MB follows pseudo-first-order kinetics.

A comparison between the rate constants of the various PC processes estimated by the fitting analysis is presented in Fig. 12. The pristine ZnO powder (ZnO-0) shows much higher PC efficiency than that of pristine TiO_2 (TiO_2-0), given that the rate constant (2.2×10^{-1} min^{-1}) of the former is almost one order of magnitude higher than that of the latter (2.5×10^{-2} min^{-1}). The superiority of ZnO-0 becomes even more evident by considering that its specific surface area (Table 1) is more than one order of magnitude smaller than that of pristine TiO_2-0. While in the vast majority of the current studies bare PC activities are compared to assess the quality of photocatalytic materials, the comparison of activities normalized by the surface area is essential for a more accurate description. The much higher PC activity of pristine ZnO powder compared to that of pristine P25 TiO_2 could be attributed to the at least two orders of magnitude higher electron mobility of ZnO compared to that of P25 TiO_2 [8].

Furthermore, the PC activity of the milled TiO_2 and ZnO samples decrease with the increase of the ball-milling time. This decrease is more pronounced in ZnO samples, given that the rate constant of ZnO-180 (9.7×10^{-3} min^{-1}) is 23 times lower than that of ZnO-0 (2.2×10^{-1} min^{-1}) whereas the rate constant of TiO_2-180 (3.4×10^{-3} min^{-1}) is 7 times lower than that of TiO_2-0 (2.5×10^{-2} min^{-1}). It is noteworthy, that the specific area of the TiO_2 samples is not substantially affected by the milling treatment whereas the corresponding one of the ZnO powders increases slightly after milling treatment (see Table 1). Once again, it is confirmed that there is no correlation between PC activities and surface

area of pristine and ball-milled TiO_2 and ZnO powders, since higher surface area leads, in general, to higher PC performances. In our case, the PC activity of all milled TiO_2 and ZnO samples decreases sharply compared to that of pristine samples (Fig. 12) and this decrease can be attributed to the high density of bulk defects produced by the mechanical ball-milling. As the above discussion of XRD, Raman and PL spectroscopies has shown, the creation of an increased bulk defect density with mechanical milling is the origin of the severely reduced PC activity of the activated powders. Indeed, bulk defects deteriorate charge carrier mobility acting as recombination sites for e-h pairs.

4. Conclusions

We have presented a detailed comparison of the influence of mechanically-induced defects on the photocatalytic activity of ZnO and TiO_2 nanopowders. Defects have an intriguing effect on photocatalysis since their nature, i.e. bulk or surface, creates a trade-off as regards the positive or negative effect they exert on PC properties. The discrimination between surface and bulk defects has to be considered with care, since several defect-probing techniques may be misinterpreted as is the case in the current literature. In this context, the assessment of the PC activity in the frame of the specific surface area or the type of the exposed crystal facets needs also reconsideration in terms of the relative fraction of bulk and surface defects.

A number of techniques were employed in the current study to scrutinize the nature of defects and correlate their amount to the observed changes of the PC activity. XRD and Raman scattering provided compatible results revealing that the amount of defects increases with the mechanical grinding time. On the contrary, PL spectra show a saturation of defect density after certain grinding time. For a rational interpretation of these results the penetration depth of each technique has to be considered. While the radiation of X-rays and the visible light excitation used in Raman scattering penetrates the whole particle size, the excitation of PL spectroscopy probes only a shell of the particles, depending on the penetration depth at this particular wavelength. Therefore, the usually envisaged correlations between certain properties, such as the PC activity, and the defect density of ZnO nanoparticles, induced either by the synthesis method or using post-growth treatment, should be considered with care. This is especially true for cases where the defect density has been estimated using only the PL spectroscopy. The PC activity of ball-milled ZnO nanoparticles, in MB degradation, decreases systematically with milling time, i.e. with the bulk defect density as estimated by Raman scattering and XRD. TiO_2 nanoparticles exhibit qualitatively different behavior under mechanical activation. Defects creation in this case is more subtle than in ZnO. The main structural changes observed pertain to the anatase-to-rutile structural transformation and partial amorphization of the crystal. The relative decrease of the PC activity of the ball milled TiO_2 particles is similar to that of the ZnO powders at short milling times, while the ZnO PC activity deteriorates faster than TiO_2 at longer milling times. Finally, the present study has provided some new insights concerning the more reliable assessment of the bulk-to-surface defects ratio and their role on the PC activity of ZnO and TiO_2.

ing Program: Thales. Investing in knowledge society through the European Social Fund.

References

[1] J. Ryu, W. Choi, Environ. Sci. Technol. 42 (2008) 294–300.
[2] X. Wang, Q. Zhang, Q. Wan, G. Dai, C. Zhou, B. Zou, J. Phys. Chem. C 115 (2011) 2769–2775.
[3] G. Veréb, Z. Ambrus, Z. Pap, Á. Kmetykó, A. Dombi, V. Danciu, A. Cheesman, K. Mogyorósi, Appl. Catal. A-Gen. 417–418 (2012) 26–36.
[4] B.M. Rajbongshi, S.K. Samdarshi, Appl. Catal. B-Environ. 144 (2014) 435–441.
[5] M.T. Qamar, M. Aslam, I.M.I. Ismail, N. Salah, A. Hameed, Chem. Eng. J. 283 (2016) 656–667.
[6] J.-M. Herrmann, Catal. Today 53 (1999) 115–129.
[7] Y. Li, W. Xie, X. Hu, G. Shen, X. Zhou, Y. Xiang, X. Zhao, P. Fang, Langmuir 26 (2010) 591–597.
[8] M. Law, L.E. Greene, J.C. Johnson, R. Saykally, P. Yang, Nat. Mater. 4 (2005) 455–459.
[9] J. Yu, X. Yu, Environ. Sci. Technol. 42 (2008) 4902–4907.
[10] B. Subash, B. Krishnakumar, M. Swaminathan, M. Shanthi, Res. Chem. Intermed. 39 (2013) 3181–3197.
[11] W. Raza, M.M. Haque, M. Muneer, Appl. Surf. Sci. 322 (2014) 215–224.
[12] W. Choi, A. Termin, M.R. Hoffmann, J. Phys. Chem. 98 (1994) 13669–13679.
[13] O. Carp, C.L. Huisman, A. Reller, Prog. Solid State Ch. 32 (2004) 33–177.
[14] S. Sakthivel, H. Kisch, Angew. Chem. Int. Ed. 42 (2003) 4908–4911.
[15] L. Ma, H. Fan, J. Wang, Y. Zhao, H. Tian, G. Dong, Appl. Catal. B-Environ. 190 (2016) 93–102.
[16] X. Zhang, J. Qin, Y. Xue, P. Yu, B. Zhang, L. Wang, R. Liu, Sci. Rep. 4 (2014) 4596.
[17] M. Kong, Y. Li, X. Chen, T. Tian, P. Fang, F. Zheng, X. Zhao, J. Am. Chem. Soc. 133 (2011) 16414–16417.
[18] T. Koida, S.F. Chichibu, A. Uedono, A. Tsukazaki, M. Kawasaki, T. Sota, Y. Segawa, H. Koinuma, Appl. Phys. Lett. 82 (2003) 532–534.
[19] H. Liu, H.T. Ma, X.Z. Li, W.Z. Li, M. Wu, X.H. Bao, Chemosphere 50 (2003) 39–46.
[20] J. Fang, H. Fan, Y. Ma, Z. Wang, Q. Chang, Appl. Surf. Sci. 332 (2015) 47–54.
[21] S. Mukhopadhyay, P.P. Das, S. Maity, P. Ghosh, P.S. Devi, Appl. Catal. B-Environ. 165 (2015) 128–138.
[22] A. Naldoni, M. Allieta, S. Santangelo, M. Marelli, F. Fabbri, S. Cappelli, C.L. Bianchi, R. Psaro, V. Dal Santo, J. Am. Chem. Soc. 134 (2012) 7600–7603.
[23] F. Zuo, L. Wang, T. Wu, Z. Zhang, D. Borchardt, P. Feng, J. Am. Chem. Soc. 132 (2010) 11856–11857.
[24] J. Wang, Z. Wang, B. Huang, Y. Ma, Y. Liu, X. Qin, X. Zhang, Y. Dai, ACS Appl. Mater. Interfaces 4 (2012) 4024–4030.
[25] J. Wang, P. Liu, X. Fu, Z. Li, W. Han, X. Wang, Langmuir 25 (2009) 1218–1223.
[26] C.A. Páez, D. Poelman, J.-P. Pirard, B. Heinrichs, Appl. Catal. B-Environ. 94 (2010) 263–271.
[27] J. Zhuang, S. Weng, W. Dai, P. Liu, Q. Liu, J. Phys. Chem. C 116 (2012) 25354–25361.
[28] D. Chen, Z. Wang, T. Ren, H. Ding, W. Yao, R. Zong, Y. Zhu, J. Phys. Chem. C 118 (2014) 15300–15307.
[29] S. Polarz, J. Strunk, V. Ischenko, M.W.E. van den Berg, O. Hinrichsen, M. Muhler, M. Driess, Angew. Chem. Int. Ed. 45 (2006) 2965–2969.
[30] H. Hu, X. Huang, C. Deng, X. Chen, Y. Qian, Mater. Chem. Phys. 106 (2007) 58–62.
[31] F. Kayaci, S. Vempati, I. Donmez, N. Biyikli, T. Uyar, Nanoscale 6 (2014) 10224–10234.
[32] T. Sagara, K. Niki, Langmuir 9 (1993) 831–838.
[33] R. Ren, Z. Yang, L.L. Shaw, J. Mater. Sci. 35 (2000) 6015–6026.
[34] A.B. Djurišić, Y.H. Leung, Small 2 (2006) 944–961.
[35] A.B. Djurišić, W.C.H. Choy, V.A.L. Roy, Y.H. Leung, C.Y. Kwong, K.W. Cheah, T.K. Gundu Rao, W.K. Chan, H. Fei Lui, C. Surya, Adv. Funct. Mater. 14 (2004) 856–864.
[36] W. Göpel, U. Lampe, Phys. Rev. B 22 (1980) 6447–6462.
[37] C.A. Arguello, D.L. Rousseau, S.P.S. Porto, Phys. Rev. 181 (1969) 1351–1363.
[38] J.M. Calleja, M. Cardona, Phys. Rev. B 16 (1977) 3753–3761.
[39] M. Šćepanović, M. Grujić-Brojčin, K. Vojisavljević, T. Srećković, J. Appl. Phys. 109 (2011) 034313.
[40] J. Wang, Q. Zhang, S. Yin, T. Sato, F. Saito, J. Phys. Chem. Solids 68 (2007) 189–192.
[41] D. Barreca, A. Gasparotto, C. Maccato, C. Maragno, E. Tondello, Surf. Sci. Spectra 14 (2007) 19–26.
[42] K. Ajay, M. Aslam, J. Phys. D: Appl. Phys. 46 (2013) 485104.
[43] M.S. Kim, Y.-S. Kim, C.H. Park, Curr. Appl. Phys. 11 (2011) S288–S291.
[44] L.K. Leah, A.R. David, S. Philip, L. Hong, W. Paul, K. Hyungchul, N. Paul, K.S. Ajaya, B. Jean-Luc, J.B. Joseph, G. Samuel, L.A.M. Oliver, J. Phys-Condens. Matter 28 (2016) 094007.
[45] R. Matzdorf, Surf. Sci. Rep. 30 (1998) 153–206.
[46] M. Krzywiecki, L. Grzadziel, A. Sarfraz, D. Iqbal, A. Szwajca, A. Erbe, Phys. Chem. Chem. Phys. 17 (2015) 10004–10013.
[47] I.K. Konstantinou, T.A. Albanis, Appl. Catal. B-Environ. 49 (2004) 1–14.